



UNIVERSIDADE ESTADUAL DE CAMPINAS  
SISTEMA DE BIBLIOTECAS DA UNICAMP  
REPOSITÓRIO DA PRODUÇÃO CIENTÍFICA E INTELECTUAL DA UNICAMP

**Versão do arquivo anexado / Version of attached file:**

Versão do Editor / Published Version

**Mais informações no site da editora / Further information on publisher's website:**

<https://www.scielo.br/j/mr/a/PVmn3vkjzTmCKmGkcfkcyWC>

**DOI: 10.1590/1980-5373-MR-2022-0038**

**Direitos autorais / Publisher's copyright statement:**

©2022 by UFSCar/Departamento de Engenharia de Materiais. All rights reserved.

DIRETORIA DE TRATAMENTO DA INFORMAÇÃO


Cidade Universitária Zeferino Vaz Barão Geraldo

CEP 13083-970 – Campinas SP

Fone: (19) 3521-6493

<http://www.repositorio.unicamp.br>

# Synthesis and Application of the Ternary $\text{Zn}_{0.5}\text{Cd}_{0.5}\text{S}/\text{ZnO}/\text{carbon}$ Xerogel Composite in the Photocatalytic Degradation of 4-chlorophenol

Gustavo Viégas Jucá Dantas<sup>a</sup>, Nicolas Perciani de Moraes<sup>a</sup>, Robson da Silva Rocha<sup>a</sup>,  
Abner de Siervo<sup>b</sup>, Marcos Roberto de Vasconcelos Lanza<sup>c</sup>, Liana Alvares Rodrigues<sup>a\*</sup> 

<sup>a</sup>Universidade de São Paulo, Escola de Engenharia de Lorena, Lorena, SP, Brasil.

<sup>b</sup>Universidade Estadual de Campinas, Instituto de Física “Gleb Wataghin”, Campinas, SP, Brasil.

<sup>c</sup>Universidade de São Paulo, Instituto de Química de São Carlos, São Carlos, SP, Brasil.

Received: January 23, 2022; Revised: March 16, 2022; Accepted: April 17, 2022

The  $\text{Zn}_{0.5}\text{Cd}_{0.5}\text{S}/\text{ZnO}/\text{carbon}$  xerogel photocatalyst was synthesized through the thermal treatment of ZnO, CdS, and a low-cost carbon xerogel matrix at high temperature (600 °C). ZnO is one of the most widely used photocatalysts, but it has low visible-light absorption, while  $\text{Zn}_{0.5}\text{Cd}_{0.5}\text{S}$  is a visible-light active photocatalyst, which can be used as a co-catalyst to enhance photoactivity under natural radiation and promote charge separation through the creation of Z-scheme heterojunctions. The further addition of the carbon xerogel can be justified by its highly developed porous structure and ability to capture photogenerated electrons, which will also promote charge separation. The creation of the hexagonal  $\text{Zn}_{0.5}\text{Cd}_{0.5}\text{S}$  and ZnO phases was confirmed through the X-ray diffractometry technique. The addition of the carbon xerogel led to an increase in the specific surface area of the XC/ZnO (630%) and XC/ZnO- $\text{Zn}_{0.5}\text{Cd}_{0.5}\text{S}$  (320%) and a decrease in particle size when compared to the pure ZnO. Regarding the photocatalytic performance of the materials, the  $\text{Zn}_{0.5}\text{Cd}_{0.5}\text{S}/\text{ZnO}/\text{carbon}$  xerogel displayed an enhanced photocatalytic activity for 4-chlorophenol degradation, with 84% degradation after 300 minutes of artificial solar irradiation. The enhanced photoactivity of the  $\text{Zn}_{0.5}\text{Cd}_{0.5}\text{S}/\text{ZnO}/\text{carbon}$  xerogel composite was further confirmed by chronoamperometry, as the composite presented higher photocurrent generation under light irradiation.

**Keywords:** Photocatalysis, carbon xerogel, zinc oxide, cadmium sulfide,  $\text{Zn}_{0.5}\text{Cd}_{0.5}\text{S}$ , 4-chlorophenol.

## 1. Introduction

Water pollution is an increasingly important issue as it can threaten both human health and the environment to a massive extent<sup>1</sup>. Wastewater-derived organic pollutants, in particular phenolic organochlorides, can be classified as compounds of special interest, due to their high toxicity, stability in natural degradation processes, and widespread use as intermediates in the production of disinfectants, pigments, and pesticides<sup>2,3</sup>. 4-chlorophenol is a typical chlorinated phenol, being used as a model in the degradation of persistent pollutants due to its high thermal and chemical stability<sup>4</sup>. Due to the potential adverse effects of severe contamination in humans (including neurological, endocrine, reproductive, and immunological risks), this compound is regulated by various environmental control agencies, including the Environmental Protection Agency (EPA–U.S.) and the World health organization (WHO), both proposing a maximum acceptable concentration of  $10 \mu\text{g L}^{-1}$ <sup>5,6</sup>. However, industrial effluents are reported to possess concentrations in the order of milligrams per liter, which highlights the dire need for efficient remediation processes<sup>7</sup>.

In this context, heterogeneous photocatalysis under solar radiation has emerged as a promising and sustainable

alternative, as it relies on a perpetual driving force to propagate the mineralization of organic pollutants<sup>8</sup>. Zinc oxide (ZnO) has been widely used to promote the photodegradation of organic pollutants since it is non-toxic, affordable, easy to synthesize, and has great mineralization capacity under ultraviolet radiation<sup>2</sup>. However, the ZnO does not absorb visible radiation in a significant manner, which hinders its viable application in solar-light-based processes<sup>9</sup>.

The creation of Z-scheme heterojunctions between semiconductors has been reported as an effective way to promote charge separation during photocatalytic activation. In this context, the coupling between ZnO and  $\text{Zn}_{0.5}\text{Cd}_{0.5}\text{S}$  is a suitable strategy to promote this kind of heterojunction, due to the staggered structure of the semiconductors' valence and conduction bands<sup>10,11</sup>. The  $\text{Zn}_{0.5}\text{Cd}_{0.5}\text{S}$  solid solution has been reported as a visible-light active structure, with superior performance to both pure ZnS and CdS, which highlights its potential application on the ZnO/ $\text{Zn}_{0.5}\text{Cd}_{0.5}\text{S}$  system<sup>12,13</sup>. As an example, the  $\text{Zn}_{0.5}\text{Cd}_{0.5}\text{S}$  has displayed good efficiency for  $\text{H}_2$  evolution ( $1250 \mu\text{mol h}^{-1}$ ) and 4-nitrophenol remediation ( $16.02 \times 10^{-2} \text{ min}^{-1}$ ) under visible light<sup>14,15</sup>. However, this structure presents high charge recombination rates, which is not ideal for photocatalytic applications<sup>14,15</sup>.

To further enhance the photocatalytic response of the ZnO/ $\text{Zn}_{0.5}\text{Cd}_{0.5}\text{S}$  system, tannin-based carbon xerogel may be

\*e-mail: [liana.r@usp.br](mailto:liana.r@usp.br)

added as a second co-catalyst, which will actively promote charge separation (due to its high conductivity) and specific surface area enlargement due to its highly developed porous structure<sup>16</sup>.

Therefore, the objective of this work is to evaluate the development of the ternary  $\text{Zn}_{0.5}\text{Cd}_{0.5}\text{S}/\text{ZnO}/\text{carbon}$  xerogel photocatalyst and its application on the degradation of 4-chlorophenol under artificial sunlight.

## 2. Materials and Methods

### 2.1. Photocatalysts synthesis

Unannealed CdS was synthesized by the same procedure described by Dantas et al.<sup>17</sup>. 4.0 g of  $\text{CdCl}_2$  (0.022 mol, 99% w/w) and 4.21 g of  $\text{Na}_2\text{S}\cdot 9\text{H}_2\text{O}$  (0.006 mol, 32-38% w/w) were dissolved in 20 mL of deionized water in separate beakers. After complete dissolution, both solutions were mixed, resulting in the precipitation of orange CdS. The precipitate was then washed until the resulting filtrate presented both  $\text{pH} = 7$  and the absence of chloride anions (monitored by  $\text{AgNO}_3$  testing). The resulting material was dried at 100 °C for 24 h and then ground and sieved through a 325-mesh sieve.

For the synthesis of  $\text{Zn}_{0.5}\text{Cd}_{0.5}\text{S}/\text{ZnO}/\text{carbon}$  xerogel photocatalyst, 8.24 g of  $\text{ZnCl}_2$  (0.06 mol, 98% w/w) and 0.5 g of PHENOTAN AP were mixed with 50 mL of deionized water (solution A). A second solution (solution B) was prepared by dissolving 6.78 g of KOH (0.1 mol, 85% w/w) in 50 mL of water. 0.546 g of previously prepared unannealed CdS (0.0038 mol) was then added to solution A, the resulting mixture being kept at 25 °C under magnetic stirring for 10 min. After the total dissolution of PHENOTAN AP in the aqueous solution, 0.5 mL of formaldehyde (0.006 mol, 37% w/w) was added to solution A. Finally, solution B was added to solution A and the material precipitated was filtered and washed with deionized water until both  $\text{pH} = 7$  and absence of chloride anions ( $\text{AgNO}_3$  testing) were observed. The material was then dried in an oven at 100 °C for 24 h, ground, and sieved through a 325-mesh sieve.

The ZnO was synthesized using the same procedure adopted for the ternary photocatalyst, with the following modifications: the exclusion of CdS, PHENOTAN AP, and formaldehyde from the synthesis. The same is valid for the  $\text{XC}/\text{ZnO}$ , which was made without the addition of the CdS component.

All resulting materials were added to closed crucibles and heat-treated in a muffle furnace with an inert  $\text{N}_2$  atmosphere at 600 °C for 30 minutes, with a heating ramp of 10 °C  $\text{min}^{-1}$ . The materials will be identified as ZnO, CdS, and  $\text{XC}/\text{ZnO}-\text{Zn}_{0.5}\text{Cd}_{0.5}\text{S}$ .

### 2.2. Characterization

The surface morphology of the materials was analyzed by scanning electron microscopy (SEM). The micrographs were obtained on a TESCAN MIRA 3 microscope, equipped with a field emission gun, using secondary electrons at 15 kV. Energy dispersive spectroscopy (EDS) was also performed, using an Oxford Instruments Swift ED3000 microanalysis system, coupled to the aforementioned scanning electron microscope.

The identification of crystalline phases was obtained by X-ray diffractometry, performed in an Empyrean Alpha-1 diffractometer with  $\text{CuK}\alpha$  radiation, in the range from 10 to 80° with a step of 0.013° and a scan speed of 0.06 s per step. The Rietveld refinement was performed using the Profex software suite<sup>18</sup>.

X-ray photoelectron spectroscopy (XPS) spectra were obtained using a SPECS Phoibos 150 hemispherical analyzer with multi-channeltron detection and  $\text{Al K}\alpha$  radiation (1486.6 eV) at constant energy setting (10 eV). Carbon tape was used to secure the powdered samples to a stainless-steel sample holder, which were then examined without further preparation. Lorentzian lines fitted to a Gaussian distribution were used in the fitting procedure. To account for the inelastic background contribution, a Shirley-type background was used. The methodology described by Wagner et al. was used to obtain the elemental concentrations. High-resolution spectra were obtained under maximum pressure of  $2 \cdot 10^{-8}$  mbar, with a pass energy of 44 eV.

Fourier Transform Infrared (FTIR) spectra were obtained by analyzing the powdered samples in a Perkin Elmer Frontier model spectrometer, using a universal attenuated total reflectance sensor (FTIR-UATR), operating in the region of 4000  $\text{cm}^{-1}$  to 450  $\text{cm}^{-1}$  with a resolution of 4  $\text{cm}^{-1}$  and 16 scans per sample.

The bandgap energies were determined by diffuse reflectance spectroscopy. The equipment used for this purpose was a Shimadzu UV-2600 spectrophotometer, equipped with an integrating sphere, with an acquisition range between 220 and 800 nm, and barium sulfate as reference material.

Porosity and surface area were determined using the Brunauer-Emmett-Teller (BET) method for  $\text{N}_2$  adsorption-desorption isotherms. Isotherms were obtained using a Gold APP Instruments V-Sorb 2800P analyzer. Before the analysis, the samples were pre-treated at 120 °C for 2h under vacuum.

An Autolab PGSTAT204 potentiostat/galvanostat was used for the chronoamperometry experiments. The following electrode system was constructed inside a 0.2 L quartz electrochemical cell: saturated  $\text{Ag}/\text{AgCl}$  reference electrode, platinum foil counter electrode, and a platinum RDE working electrode. A 0.1 mol  $\text{L}^{-1}$   $\text{K}_2\text{SO}_4$  aqueous electrolyte was employed throughout the experiments. The photocurrent generation was measured at 0.4 V (versus  $\text{Ag}/\text{AgCl}$ ). A porous microlayer of each material was deposited on the platinum surface of the working electrode, which was then illuminated by an artificial solar light source (Osram Ultra Vitalux 300 W).

### 2.3. Photocatalytic evaluation

The photocatalytic activity of the materials was evaluated using 0.1 g of photocatalyst in 500 mL of a 10 mg  $\text{L}^{-1}$  4-chlorophenol (4-CP) solution. The tests were conducted at  $\text{pH} = 5.5$ , which is the one found for the deionized water used. The reactor consisted of a jacketed beaker connected to a thermostatic bath set to 25 °C. The solution was kept in the dark until the adsorption-desorption equilibrium was reached. Each sample collected from the reactional medium was filtered through a nylon syringe filter and the 4-chlorophenol concentration was determined using a Shimadzu UV-2600 series UV-Vis spectrophotometer,

set to 224 nm wavelength. After the adsorption-desorption equilibrium was reached, the artificial solar radiation was activated and the reaction was monitored at predetermined intervals for 300 minutes. The light source used was an Ultravitalux Osram lamp (300 W, positioned 10 cm above the reactor's surface with a photon flux of  $1950 \mu\text{mol photons m}^{-2} \text{ s}^{-1}$ ), designed to simulate the solar emission spectrum. Furthermore, the mineralization of the 4-chlorophenol at the end of the experiment was evaluated via total organic carbon (TOC) measurement using Shimadzu VCSN TOC equipment. A Shimadzu HPLC model LC-20 AT was used to validate the 4-CP degradation, with a Phenomenex Luna C-18 column and a mobile phase composed of 30% water and 70% acetonitrile. A flow of  $1 \mu\text{L min}^{-1}$  was used, with an injection volume of  $20 \mu\text{L}$  and a retention time of 10 min. The concentration of the 4-CP was determined by a UV-detector, at the wavelength of 224 nm. Recycling tests were performed to assess the stability of the ternary material after multiple photocatalytic cycles. Mechanistic evaluation for active radicals generation was performed using the scavenging methodology. The scavengers used were potassium chromate (electron scavenger), sodium oxalate (hole scavenger), isopropyl alcohol (hydroxyl radical scavenger), and  $\text{N}_2$  (which depletes  $\text{O}_2$  gas in solution, halting the production of superoxide radicals).

Figure 1 shows the schematic representation of the reactional system.

### 3. Results and Discussion

#### 3.1. Characterization

The diffraction patterns of the materials are presented in Figure 2.

The ZnO and XC/ZnO diffractograms display peaks at  $31.9^\circ$ ,  $34.7^\circ$ ,  $36.5^\circ$ ,  $47.8^\circ$ ,  $56.8^\circ$ ,  $63.1^\circ$ ,  $66.4^\circ$ ,  $67.9^\circ$  and  $69.1^\circ$ , while the XRD pattern of CdS show peaks at  $24.8^\circ$ ,  $26.5^\circ$ ,  $28.2^\circ$ ,  $36.7^\circ$ ,  $43.7^\circ$ ,  $47.9^\circ$ ,  $50.9^\circ$ ,  $51.9^\circ$  and  $52.9^\circ$ . In both cases these peaks are characteristic of the hexagonal phase of each

semiconductor, with the respective reflection planes: (1 0 0), (0 0 2), (1 0 1), (1 0 2), (1 1 0), (1 0 3), (2 0 0), (1 1 2) and (2 0 1)<sup>16,19</sup>. The ternary material (XC/ZnO- $\text{Zn}_{0.5}\text{Cd}_{0.5}\text{S}$ ) also presents the peaks related to the hexagonal phase of ZnO. However, the peaks at  $25.9^\circ$ ,  $27.6^\circ$ ,  $29.4^\circ$ ,  $38.1^\circ$ ,  $45.5^\circ$ ,  $49.6^\circ$ , and  $53.9^\circ$  correspond to the hexagonal phase of  $\text{Zn}_{0.5}\text{Cd}_{0.5}\text{S}$ , evidencing the formation of a solid solution instead of a simple mixture of materials<sup>20</sup>. The Rietveld refinement results indicated that the mass composition regarding the crystalline phases of the XC/ZnO- $\text{Zn}_{0.5}\text{Cd}_{0.5}\text{S}$  sample can be defined as 91.69% of ZnO and 8.31% of  $\text{Zn}_{0.5}\text{Cd}_{0.5}\text{S}$  ( $\chi^2=2.3$ ).

The micrographs for the materials are presented in Figure 3.

Figure 3a shows that CdS presents is composed of large particles, which are formed due to the coalescence of CdS particles under thermal annealing<sup>17</sup>. Figure 3b illustrates that the morphology of ZnO is composed of nodular particles with spherical tendency. Figure 3c and 3d, however, show that the materials containing carbon xerogel are composed of small nodular particles and plaques, evidencing a significant morphological change in comparison to the pure ZnO and CdS. Thus, the presence of carbon xerogel led to a reduction in the size of ZnO particles, as the tannin-formaldehyde xerogel particles can work as active sites for the nucleation of the zinc hydroxide, resulting in smaller grain sizes<sup>3</sup>. This reduced particle size may enhance the photocatalytic activity of the samples, as a larger surface area is available for the photoactivation process.

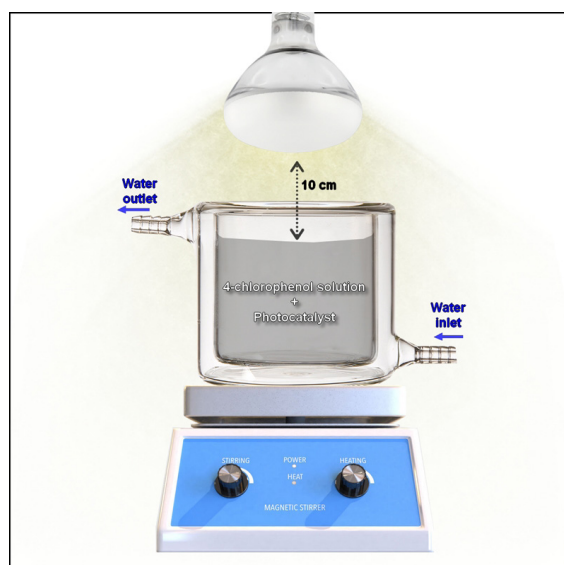


**Figure 1.** Reactional system used for the photocatalytic tests.

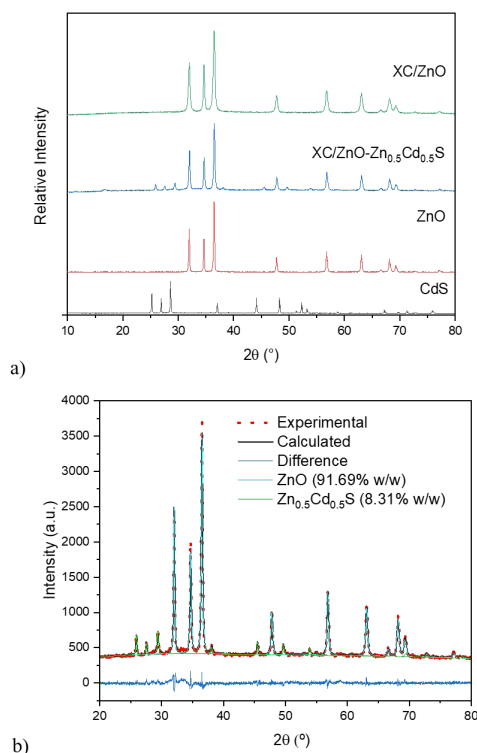


**Figure 2.** a) Diffraction patterns of the materials ZnO, XC/ZnO, CdS, and XC/ZnO- $\text{Zn}_{0.5}\text{Cd}_{0.5}\text{S}$ ; b) Rietveld refinement of the XC/ZnO- $\text{Zn}_{0.5}\text{Cd}_{0.5}\text{S}$  diffractogram.



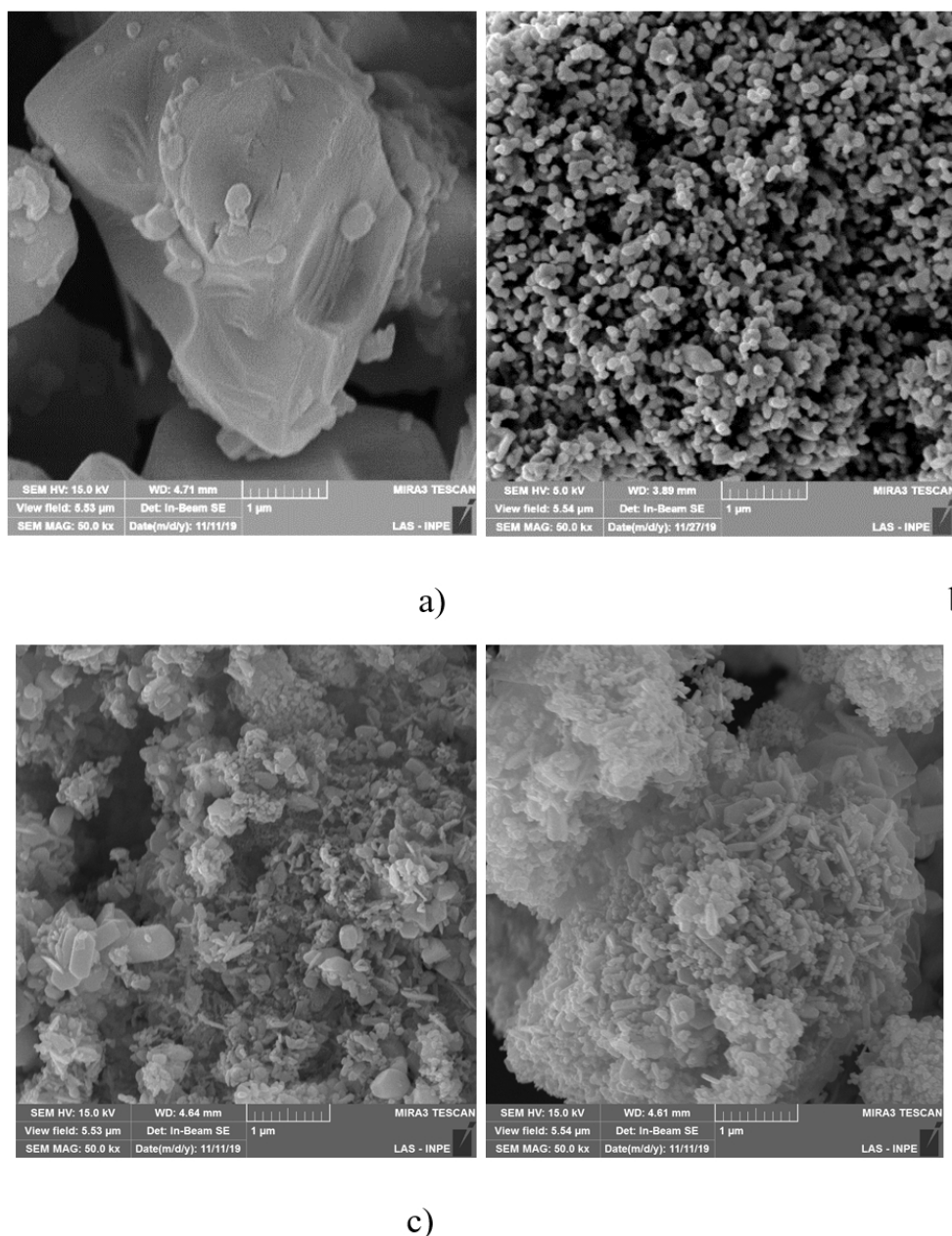


**Figure 3.** Micrographs with 50.000x magnification for the materials: a) CdS; b) ZnO; c) XC/ZnO; d) XC/ZnO-Zn<sub>0.5</sub>Cd<sub>0.5</sub>S.

The XPS spectra for XC/ZnO-Zn<sub>0.5</sub>Cd<sub>0.5</sub>S are presented in Figure 4.

The peaks in Figure 4a were deconvoluted and found to correspond to cadmium's 3d<sub>3/2</sub> (412 eV) and 3d<sub>5/2</sub> (406 eV) energy levels<sup>21</sup>. Similarly, the peaks in Figure 4b correspond to zinc's 2p<sub>1/2</sub> (1,045 eV) and 2p<sub>3/2</sub> (1,022 eV) energy levels<sup>16</sup>.

The experimental data in Figure 4c was deconvoluted into four different peaks relating to carbon bonds, with the smallest peak being representative of carboxyl groups (O-C=O bonds) at 289.4 eV. There is also a small peak related to C-OH bonds at 286.7 eV. Both of these small peaks are present at their typical energy range<sup>22</sup>. The main

peak is representative of carbon-carbon bonds at 284.4 eV; it's hard to distinguish simple from double bonds except in high ordered materials and the peak could fit into both cases<sup>22</sup>. The final peak at 285.3 eV fits as representative of both C-O bonds and C-O-Zn bonds<sup>16,22</sup>.

The O 1s spectrum peak in Figure 4d was deconvoluted into four peaks. The main component is a lower energy band (530.9 eV) related to the ZnO-wurtzite structure<sup>23</sup>. There are also higher energy components (532, 533, and 534 eV) related to C-O bonds, organic functional groups, hydroxyl groups, and adsorbed oxygen, respectively<sup>16,23</sup>. The S 2p spectrum, even if present at the survey spectrum, was not shown due

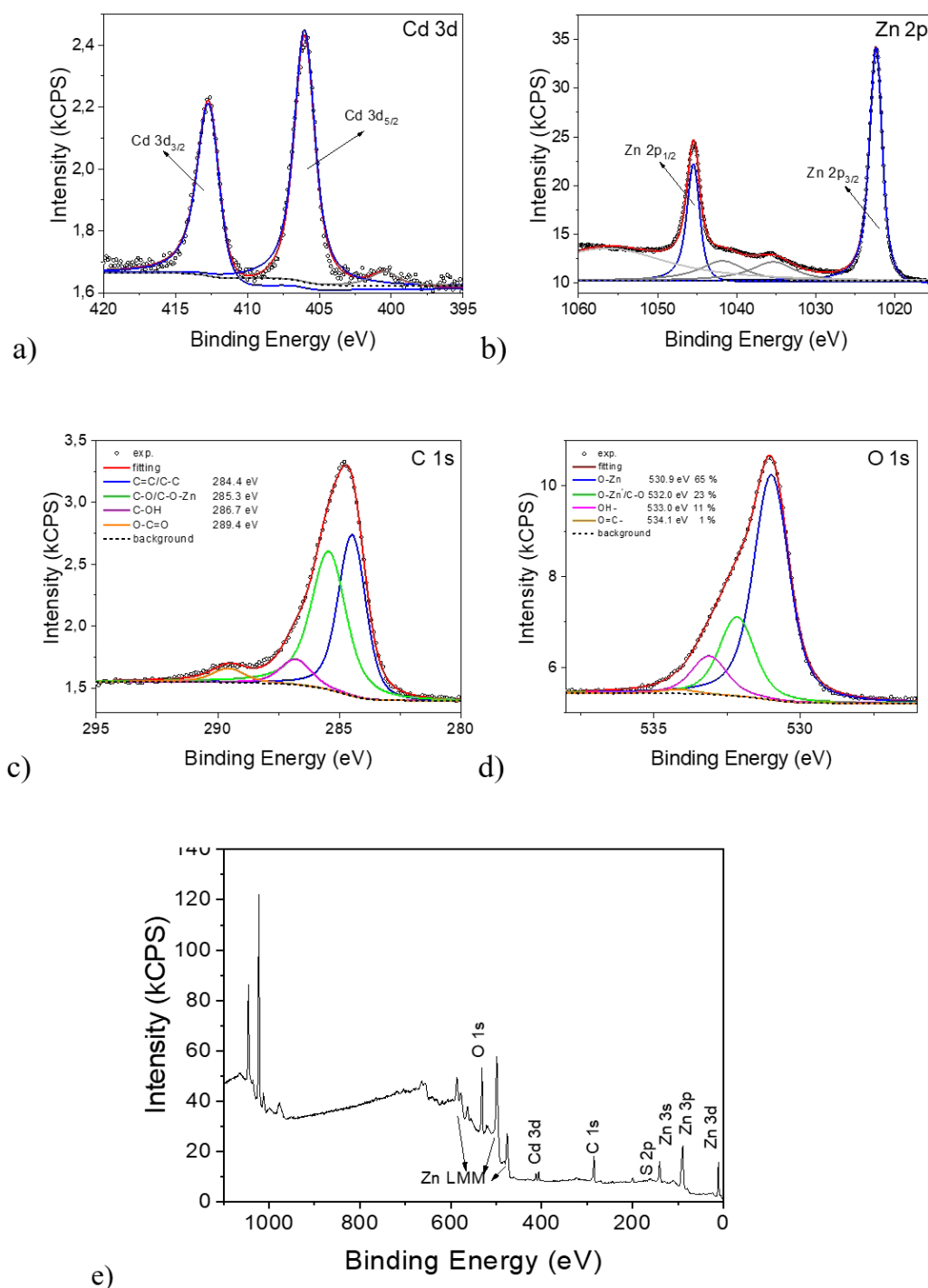


**Figure 4.** XPS spectra of the XC/ZnO- $\text{Zn}_{0.5}\text{Cd}_{0.5}\text{S}$ : a) Cd 3d; b) Zn 2p; c) C 1s; d) O 1s and e) Survey spectrum.

to the elevated amount of background noise observed in the analysis, which made a proper evaluation unfeasible.

Figure 5 shows the elemental distribution of the material XC/ZnO- $\text{Zn}_{0.5}\text{Cd}_{0.5}\text{S}$ , whereas Table 1 shows the atomic composition of the sample.

As Figure 5 shows, the carbon elemental distribution in the XC/ZnO- $\text{Zn}_{0.5}\text{Cd}_{0.5}\text{S}$  is considerably homogeneous, which is likely to facilitate the charge transfer within the

heterojunction formed among carbonaceous and inorganic phases<sup>24</sup>. Furthermore, some concentration points of cadmium and sulfur can be observed, which is expected as the CdS was not co-precipitated along with the ZnO, being added to the synthesis as a powder; however, a good diffusion of the Cd and S elements was obtained throughout the composite's surface, likely due to the thermal treatment process employed. Regarding the composition of the sample, the values obtained

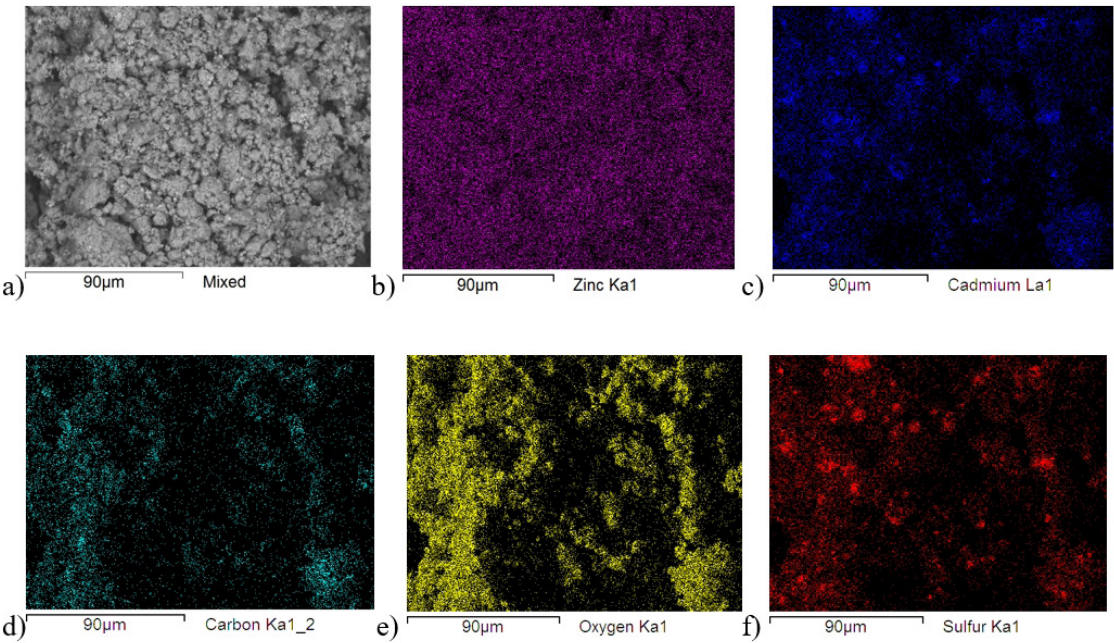


**Figure 5.** Elemental distribution of the material XC/ZnO-Zn<sub>0.5</sub>Cd<sub>0.5</sub>S: a) Original SEM; b) Zinc; c) Cadmium; d) Carbon; e) Oxygen and f) Sulfur.

**Table 1.** Atomic composition of the XC/ZnO-Zn<sub>0.5</sub>Cd<sub>0.5</sub>S material.

Element	Weight %	Atomic %
Carbon	12.112	29.633
Oxygen	22.553	41.426
Sulfur	1.780	1.631
Zinc	56.849	25.556
Cadmium	6.707	1.753

are consistent with the composition defined by Rietveld refinement, with the additional information for carbon content, which is approximately 12%.

Absorbance spectra are presented in Figure 6a, while the Tauc plot for the different materials is presented in Figure 6b.

As expected, the ZnO presents almost zero absorbance at visible light wavelengths higher than 500 nm, its absorption limited to the UV region. CdS absorbs radiation in the UV and visible regions, absorbing radiation wavelengths up to 550 nm. The presence of carbon xerogel in ternary material markedly increases the absorption of radiation in the visible light spectrum, as expected due to the optical properties observed by Moraes et al. in previous work<sup>25</sup>. Using the Tauc relation (Equation 1), the bandgap of each material was calculated from the associated absorption spectra<sup>26</sup>.

$$\frac{1}{(ah\nu)^m} = B(h\nu - E_{gap}) \tag{1}$$

where  $\alpha$  is the absorption coefficient;  $h$  is the Planck constant,  $\nu$  is the photon's frequency,  $B$  is a constant,  $E_{gap}$  is the bandgap energy, and  $m$  defines the type of transition (in this case,  $m = 0.5$  for direct transition). The  $E_{gap}$  parameter can then be obtained by the extrapolation of the linear region of the  $(ah\nu)^{1/m}$  plot to  $y = 0$ .

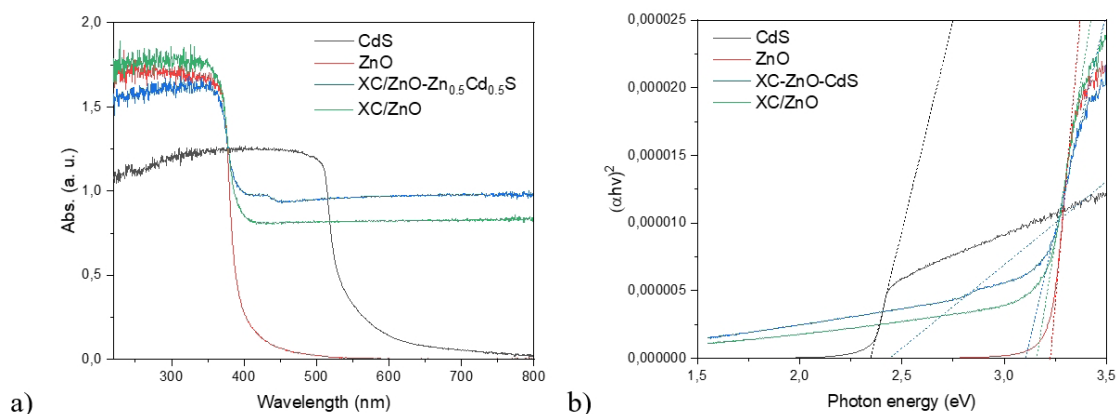
From the Tauc plots, it can be observed that the bandgap energy of ZnO is 3.21 eV, which is characteristic of such a structure<sup>27</sup>. As expected, CdS has the lowest bandgap energy at 2.36 eV, which is within the range determined by the literature<sup>28</sup>. The material XC/ZnO presented a slight reduction in the bandgap value, 3.17 eV, which is likely due to the carbon incorporation into the ZnO structure. However, the ternary material has two bandgap energies, at 2.45 eV and 3.13 eV. Those two energies relate to the presence of the different semiconductors in the material, with the lower energy relating to the presence of Zn<sub>0.5</sub>Cd<sub>0.5</sub>S, while the higher energy relates to the presence of ZnO<sup>16,29</sup>.

The isotherms of the different materials are presented in Figure 7.

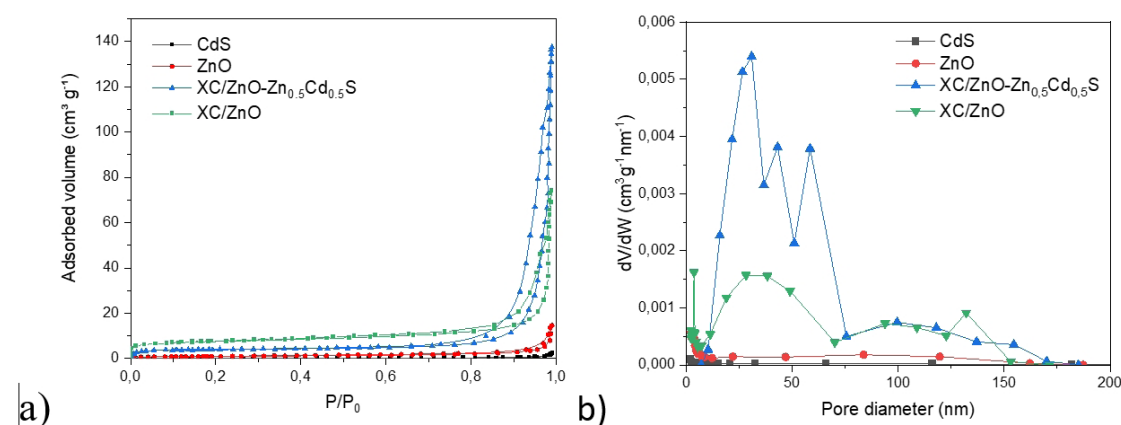
All the materials present IUPAC isotherms type IV, with H3 type hysteresis. Materials with IV-H3 isotherms typically don't present adsorption limits at high P/P<sub>0</sub> ratios, due to their constitution of plate-like aggregate structures, with slit-shaped pores<sup>30</sup>.

Table 2 presents the morphological parameters obtained for the materials.

Of all the materials, CdS presented both the lowest pore volume (0.004 cm<sup>3</sup> g<sup>-1</sup>) and lowest surface area (0.28 m<sup>2</sup> g<sup>-1</sup>). ZnO displayed intermediate pore volume (0.023 cm<sup>3</sup> g<sup>-1</sup>) and surface area (3.3 m<sup>2</sup> g<sup>-1</sup>). The ternary material presents the highest pore volume (0.226 cm<sup>3</sup> g<sup>-1</sup>) and intermediate surface area (14.2 m<sup>2</sup> g<sup>-1</sup>), which is due to the combined effect of the carbon xerogel and CdS in the material, corroborating the morphological modification observed in the scanning electron micrograph of the material (Figure 3d). Regarding the pore size distribution, it is clear that the XC/ZnO-Zn<sub>0.5</sub>Cd<sub>0.5</sub>S possesses a much more developed mesoporous network than the materials without the carbon xerogel, which is expected



**Figure 6.** a) Absorbance spectra for the ZnO, CdS, and XC/ZnO-Zn<sub>0.5</sub>Cd<sub>0.5</sub>S; b) Tauc plot for the ZnO, CdS, and XC/ZnO-Zn<sub>0.5</sub>Cd<sub>0.5</sub>S.



**Figure 7.** a) Nitrogen isotherms for the ZnO, CdS, and XC/ZnO-Zn<sub>0.5</sub>Cd<sub>0.5</sub>S; b) Pore diameter distribution for the ZnO, CdS, and XC/ZnO-Zn<sub>0.5</sub>Cd<sub>0.5</sub>S.

**Table 2.** Morphological parameters obtained for the materials.

Material	Specific surface area (m <sup>2</sup> g <sup>-1</sup> )	Micropore area (m <sup>2</sup> g <sup>-1</sup> )	Pore volume (cm <sup>3</sup> g <sup>-1</sup> )	Micropore volume (cm <sup>3</sup> g <sup>-1</sup> )
XC/ZnO-Zn <sub>0.5</sub> Cd <sub>0.5</sub> S	14.1	10.3	0.21	0.004
XC/ZnO	25.5	12.9	0.11	0.006
ZnO	3.34	0.85	0.022	0.0003
CdS	0.28	0.15	0.004	0.0001

due to the highly porous nature of this carbonaceous structure. The XC/ZnO, on the other hand, has a higher number of pores in the region between 0-10 nm, which agrees with its higher specific surface area and intermediate pore volume.

### 3.2. Photocatalytic tests

The results of the photocatalytic tests under artificial solar light are presented in Figure 8.

Firstly, it is necessary to point out that only the XC/ZnO-Zn<sub>0.5</sub>Cd<sub>0.5</sub>S and XC/ZnO presented 4-chlorophenol adsorption capacities, which were of 5 mg g<sup>-1</sup> for both materials (achieved after 30 min). The ternary material

presented the best photocatalytic performance among the materials evaluated, degrading approximately 84% of the 4-chlorophenol in the solution after 5h. The XC/ZnO presented the second-best 4-chlorophenol degradation percentage (75%), while the pure ZnO and CdS presented degradation efficiencies of 70% and 27%, respectively. These results show the beneficial effects of the carbon xerogel and Zn<sub>0.5</sub>Cd<sub>0.5</sub>S coupling in ZnO photoactivity, which can be defined as:

- Increase in surface area, which led to the optimization of the interface available for superficial processes, such as the adsorption and reaction steps of the photocatalytic mechanism



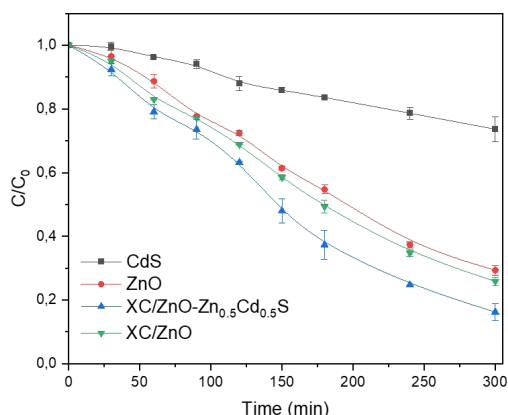


**Figure 8.** Solar light photocatalytic tests for the materials.

- ii) Formation of Z-scheme heterojunctions and carbon/semiconductor heterojunctions, facilitating the transport of photogenerated charges during the process and, therefore, hindering the recombination process.
- iii) Reduction of the bandgap energy, which probably led to an increased photocatalytic efficiency under the simulated sunlight applied to the system

Furthermore, all materials presented good reproducibility for the degradation of 4-chlorophenol. The results of the total organic carbon content showed a reduction of approximately 60% at the end of the experiment using the ternary material, indicating that 60% of the 4-chlorophenol was completely mineralized into water, CO<sub>2</sub>, and inorganic components during the photocatalytic test.

Employing the photocatalytic data collected, the kinetic evaluation of the photodegradation reaction was evaluated using a simplified Langmuir-Hinshelwood pseudo-first-order model, as described by Equation 2<sup>30</sup>.

$$\ln\left(\frac{C}{C_0}\right) = -k_{app}t \quad (2)$$

Where  $C$  is the 4-chlorophenol concentration at a given time  $t$ ,  $C_0$  is the concentration at the adsorption equilibrium ( $t=0$ ) and  $k_{app}$  is the apparent reaction rate constant, given in min<sup>-1</sup>.

Table 3 shows the parameters gathered after the kinetic modeling.

The results show that the photocatalytic degradation of the 4-chlorophenol is suitably described by the proposed model, as the R<sup>2</sup> values are fairly close to 1. Furthermore, the XC/ZnO-Zn<sub>0.5</sub>Cd<sub>0.5</sub>S obtained the highest  $k_{app}$  value among the materials studied, confirming its superior photocatalytic activity for the 4-chlorophenol degradation under simulated sunlight.

The photocatalytic efficiency of the ternary material for multiple cycles of 4-chlorophenol degradation is shown in Figure 9a, while the active radical generation mechanism is evaluated in Figure 9b.

As can be seen in Figure 9a, the ternary material presented good stability to multiple photocatalytic cycles, losing close to 5% of efficiency after four photocatalytic cycles.

**Table 3.** Kinetic parameters obtained for the photodegradation tests.

Material	$k_{app}$ (min <sup>-1</sup> )	R <sup>2</sup>
ZnO	0.0037	0.98
CdS	0.0011	0.99
XC/ZnO	0.0047	0.98
XC/ZnO-Zn <sub>0.5</sub> Cd <sub>0.5</sub> S	0.0057	0.98

From the mechanism tests (Figure 9b), it can be noted that isopropyl alcohol consistently suppresses the 4-CP degradation provided by the ZnO, XC/ZnO, and ternary material, which suggests the degradation pathway for these materials is mediated mainly by the formation of hydroxyl radicals. As the valence band of the Zn<sub>0.5</sub>Cd<sub>0.5</sub>S is not high enough to promote the generation of hydroxyl radical (2.08 eV), this result indicates that the vacancies formed during the photocatalytic process are concentrated in the ZnO valence band (2.87 eV), which in turn indicates the formation of a Z-scheme mechanism for charge transfer<sup>31</sup>. On the other hand, in the case of CdS, the hydroxyl radical does not participate in the 4-CP degradation, as the valence band potential of CdS (1.95 eV) is lower than that required for the hydroxyl radical formation (2.32 eV)<sup>32</sup>. For CdS, the electrons play an important role in 4-CP degradation by acting in the formation of the superoxide radical (responsible for 4-CP degradation)<sup>33</sup>.

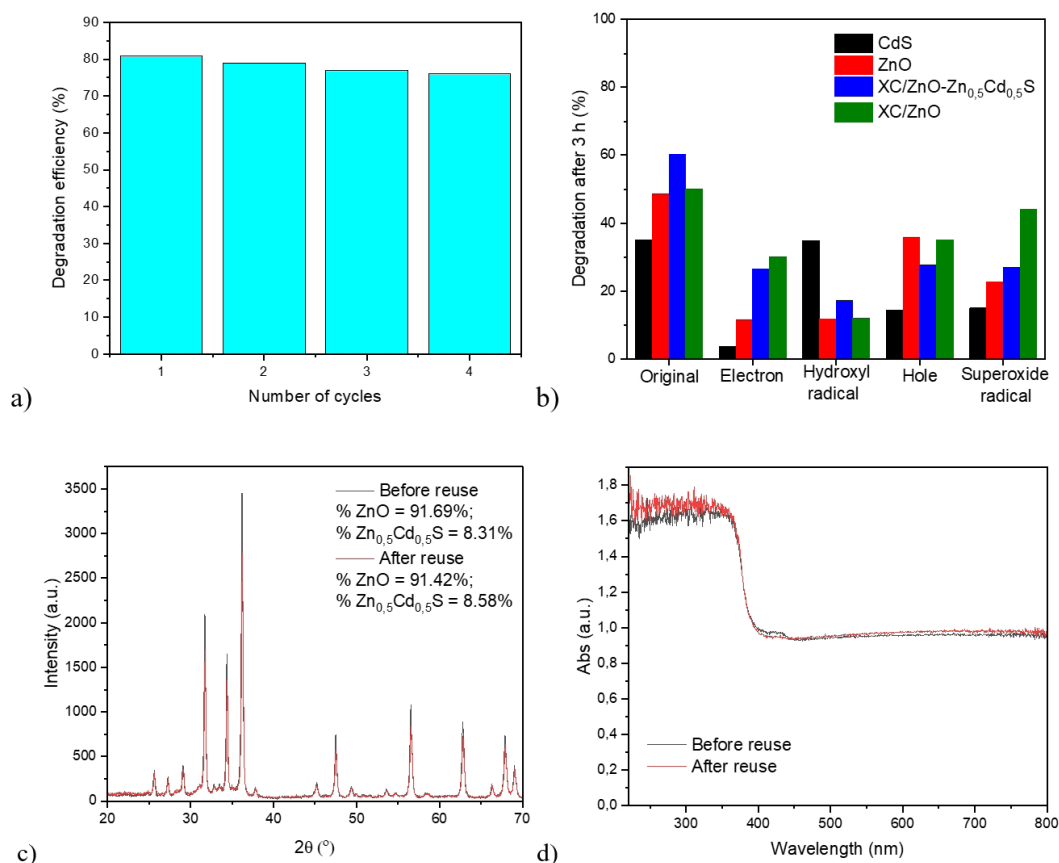
As for the stability of the XC/ZnO-Zn<sub>0.5</sub>Cd<sub>0.5</sub>S sample, Figure 9c and Figure 9d show that no major modification was observed in the optical and structural properties of the composite, indicating that the constituent phases were not degraded or modified in any significant form.

Figure 10a shows the results obtained by HPLC for the aliquots collected during the photodegradation experiment using the XC/ZnO-Zn<sub>0.5</sub>Cd<sub>0.5</sub>S, whereas Figure 10b shows the absorption spectra of the same aliquots.

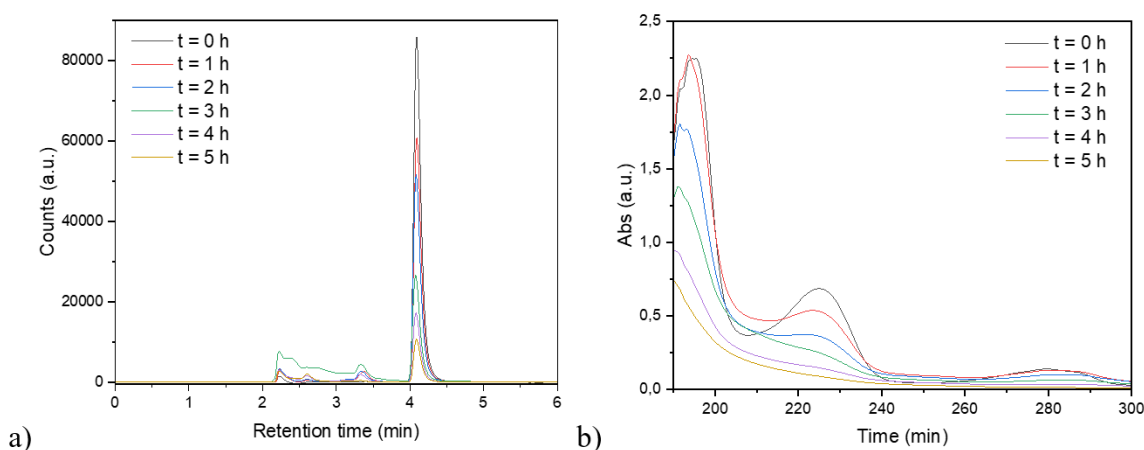
The HPLC results obtained show the formation of several intermediates during the photocatalytic degradation of the 4-CP, with a peak signal at  $t = 3$  h. Observing the absorption spectrum of the samples, it is noticeable that an increase in absorption occurs between the wavelengths of 200–220 nm and 240–270 nm during the experiment, suggesting that the intermediates formed are 4-chlorocatechol, benzoquinone, and hydroquinone<sup>34,35</sup>. It is also clear that the intensity of the signals attributed to the intermediates is quite low at the end of the experiments, corroborating the fact that most of the 4-chlorophenol was mineralized after 5 h of light irradiation. Furthermore, the 4-CP concentrations obtained using the HPLC method were consistent with the ones found by spectrophotometry, indicating that both methods can be used effectively to determine the concentration of 4-CP in the photocatalytic tests.

Figure 11 shows the chronoamperometry results for the materials developed

As the results show, the ternary material has an enhanced current generation capacity under simulated solar light, which agrees with the results obtained in the photocatalytic tests. This behavior can be linked to the facilitated charge transport induced by the heterojunctions between



**Figure 9.** a) Recycling tests for the ternary material; b) Evaluation of the mechanism of active radical formation; c) XRD results after reuse for the XC/ZnO- $\text{Zn}_{0.5}\text{Cd}_{0.5}\text{S}$ ; d) Diffuse reflectance results after reuse for the XC/ZnO- $\text{Zn}_{0.5}\text{Cd}_{0.5}\text{S}$ .



**Figure 10.** a) HPLC results for the test using XC/ZnO- $\text{Zn}_{0.5}\text{Cd}_{0.5}\text{S}$ ; b) Absorption spectra of the aliquots collected during the tests using XC/ZnO- $\text{Zn}_{0.5}\text{Cd}_{0.5}\text{S}$ .

the components of the composite, which effectively worked toward the optimization of the photocatalytic response obtained by the XC/ZnO- $\text{Zn}_{0.5}\text{Cd}_{0.5}\text{S}$ .<sup>30</sup>

Finally, Figure 12 shows a schematic representation of the heterojunctions formed in the structure of the XC/ $\text{ZnO}-\text{Zn}_{0.5}\text{Cd}_{0.5}\text{S}$  ternary composite.

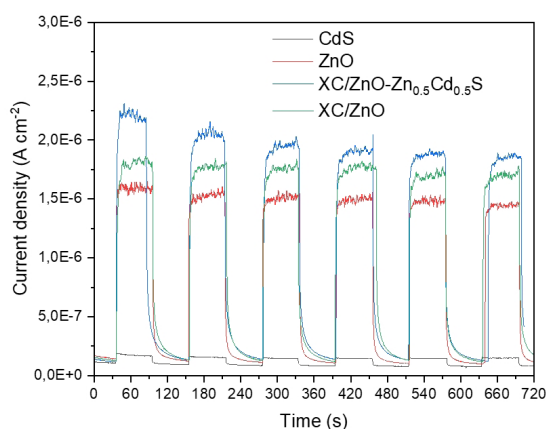


Figure 11. Chronoamperometry results for the materials synthesized.

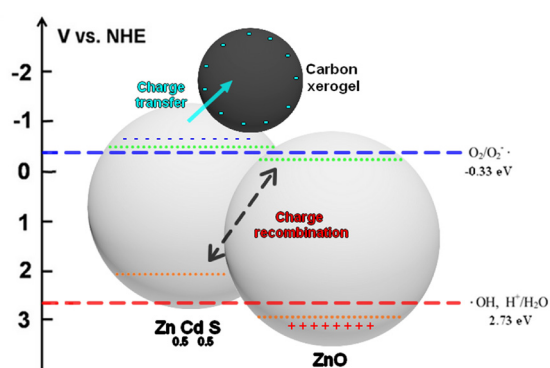


Figure 12. Schematic representation of the heterojunctions present in the XC/ZnO-Zn<sub>0.5</sub>Cd<sub>0.5</sub>S ternary composite.

## 4. Conclusions

The characterization of the materials synthesized proved the efficient formation of the Zn<sub>0.5</sub>Cd<sub>0.5</sub>S solid solution in the ternary composite due to the thermal treatment process. Furthermore, the addition of the carbon xerogel led to several morphological modifications, such as a decreased particle size and increased specific surface area. The optical properties of the XC/ZnO-Zn<sub>0.5</sub>Cd<sub>0.5</sub>S composite suggested an enhanced visible light absorption capacity due to the incorporation of the Zn<sub>0.5</sub>Cd<sub>0.5</sub>S and carbon xerogel to the ZnO. As for the photocatalytic performance, the XC/ZnO-Zn<sub>0.5</sub>Cd<sub>0.5</sub>S was shown to possess a significantly enhanced photocatalytic activity when compared to its pure semiconductor components, which can be attributed to its higher specific surface area and porosity, higher visible light absorption, and facilitated charge transfer due to both the Z-scheme heterojunctions between semiconductors the heterojunctions between semiconductors and carbon xerogel. The chronoamperometry tests confirmed the superior photocurrent generation of the ternary material, whereas the mechanism evaluation showed that the hydroxyl radical was the main component for the photodegradation of the 4-chlorophenol molecule in the tests performed using the XC/ZnO-Zn<sub>0.5</sub>Cd<sub>0.5</sub>S.

## 5. Acknowledgments

The authors acknowledge the support provided by São Paulo Research Foundation (FAPESP) (Grants 2018/10492-1 and 2018/16360-0) and by the Coordenação de Aperfeiçoamento de Pessoal de Nível Superior - Brasil (CAPES) - Finance Code 001.

## 6. References

- Byrne C, Subramanian G, Pillai SC. Recent advances in photocatalysis for environmental applications. *J Environ Chem Eng.* 2018;6(3):3531-55.
- Lee KM, Lai CW, Ngai KS, Juan JC. Recent developments of zinc oxide based photocatalyst in water treatment technology: a review. *Water Res.* 2016;88:428-48. <http://dx.doi.org/10.1016/j.watres.2015.09.045>
- Moraes NP, Valim RB, Rocha RS, Silva MLCP, Campos TMB, Thim GP, et al. Effect of synthesis medium on structural and photocatalytic properties of ZnO/carbon xerogel composites for solar and visible light degradation of 4-chlorophenol and bisphenol A. *Colloids Surf A Physicochem Eng Asp.* 2020;584:124034.
- Song R, Chi H, Ma Q, Li D, Wang X, Gao W, et al. Highly efficient degradation of persistent pollutants with 3D nanocone TiO<sub>2</sub>-based photoelectrocatalysis. *J Am Chem Soc.* 2021;143(34):13664-74.
- Kurian M, Nair DS. Heterogeneous Fenton behavior of nano nickel zinc ferrite catalysts in the degradation of 4-chlorophenol from water under neutral conditions. *J Water Process Eng.* 2015;8:e37-49.
- Salehi H, Ebrahimi AA, Ehrampoush MH, Salmani MH, Fard RF, Jalili M, et al. Integration of photo-oxidation based on UV/Persulfate and adsorption processes for arsenic removal from aqueous solutions. *Groundw Sustain Dev.* 2020;10:100338. <https://doi.org/10.1016/j.gsd.2020.100338>
- Sahinkaya E, Dilek FB. Effect of biogenic substrate concentration on the performance of sequencing batch reactor treating 4-CP and 2,4-DCP mixtures. *J Hazard Mater.* 2006;128(2-3):258-64.
- Ge J, Zhang Y, Park SJ. Recent advances in carbonaceous photocatalysts with enhanced photocatalytic performances: a mini review. *Materials.* 2019;12(12):1916.
- Lam SM, Sin JC, Abdullah AZ, Mohamed AR. Degradation of wastewaters containing organic dyes photocatalysed by zinc oxide: a review. *Desalination Water Treat.* 2012;41(1-3):131-69.
- Anusuyadevi PR. *Synthesis of novel nanophotocatalyst in micro/millifluidic supercritical reactor* [thesis]. Bordeaux: Université de Bordeaux; 2019.
- Moraes NP, Rocha RS, Silva MLCP, Campos TMB, Thim GP, Landers R, et al. Facile preparation of Bi-doped ZnO/β-Bi<sub>2</sub>O<sub>3</sub>/Carbon xerogel composites towards visible-light photocatalytic applications: effect of calcination temperature and bismuth content. *Ceram Int.* 2020;46(15):23895-909.
- Zhao H, Liu H, Sun R, Chen Y, Li XA. Zn<sub>0.5</sub>Cd<sub>0.5</sub>S Photocatalyst modified by 2d black phosphorus for efficient hydrogen evolution from water. *ChemCatChem.* 2018;10(19):4395-405.
- Dai D, Xu H, Ge L, Han C, Gao Y, Li S, et al. In-situ synthesis of CoP co-catalyst decorated Zn<sub>0.5</sub>Cd<sub>0.5</sub>S photocatalysts with enhanced photocatalytic hydrogen production activity under visible light irradiation. *Appl Catal B.* 2017;217:429-36. <http://dx.doi.org/10.1016/j.apcatb.2017.06.014>
- Sun R, Song J, Zhao H, Li X. Control on the homogeneity and crystallinity of Zn<sub>0.5</sub>Cd<sub>0.5</sub>S nanocomposite by different reaction conditions with high photocatalytic activity for hydrogen production from water. *Mater Charact.* 2018;144(July):57-65. <http://dx.doi.org/10.1016/j.matchar.2018.06.033>
- Debnath B, Dhingra S, Sharma V, Krishnan V, Nagaraja CM. Efficient photocatalytic generation of hydrogen by twin Zn<sub>0.5</sub>Cd<sub>0.5</sub>S nanorods decorated with noble metal-free co-

- catalyst and reduction of 4-nitrophenol in water. *Appl Surf Sci.* 2021;550:149367. <http://dx.doi.org/10.1016/j.apsusc.2021.149367>
16. Moraes NP, Bacetto LA, Santos GS, Silva MLCP, Machado JPB, Campos TMB, et al. Synthesis of novel ZnO/carbon xerogel composites: effect of carbon content and calcination temperature on their structural and photocatalytic properties. *Ceram Int.* 2019;45(3):3657-67. <http://dx.doi.org/10.1016/j.ceramint.2018.11.027>
17. Dantas GVJ, Moraes NP, Bacani R, Rodrigues LÁ. Facile synthesis of cadmium sulfide and the effect of thermal annealing in N<sub>2</sub>-rich atmosphere on its structural, morphological, chemical, and optical properties. *Mater Chem Phys.* 2021;2022:277.
18. Doebelin N, Kleeberg R. Profex: a graphical user interface for the Rietveld refinement program BGMN. *J Appl Cryst.* 2015;48:1573-80.
19. Heiba ZK, Mohamed MB, Mostafa NY. Effect of V and Y doping on the structural, optical and electronic properties of CdS (hexagonal and cubic phases). *Appl Phys, A Mater Sci Process.* 2019;125(2):1-12. <http://dx.doi.org/10.1007/s00339-019-2428-9>
20. Gong H, Hao X, Jin Z, Ma Q. WP modified S-scheme  $\text{Zn}_{0.5}\text{Cd}_{0.5}\text{S}/\text{WO}_3$  for efficient photocatalytic hydrogen production. *New J Chem.* 2019;43(48):19159-71.
21. Mazón-Montijo DA, Sotelo-Lerma M, Rodríguez-Fernández L, Huerta L. AFM, XPS and RBS studies of the growth process of CdS thin films on ITO/glass substrates deposited using an ammonia-free chemical process. *Appl Surf Sci.* 2010;256(13):4280-7.
22. Chen X, Wang X, Fang D. A review on C1s XPS-spectra for some kinds of carbon materials. *Fuller Nanotub Carbon Nanostructures.* 2020;28(12):1048-58. <http://dx.doi.org/10.1080/1536383X.2020.1794851>
23. Mishra DK, Mohapatra J, Sharma MK, Chattarjee R, Singh SK, Varma S, et al. Carbon doped ZnO: synthesis, characterization and interpretation. *J Magn Magn Mater.* 2013;329:146-52. <http://dx.doi.org/10.1016/j.jmmm.2012.09.058>
24. Low J, Yu J, Jaroniec M, Wageh S, Al-Ghamdi AA. Heterojunction photocatalysts. *Adv Mater.* 2017;29(20)
25. Moraes NP, Goes CM, Rocha R S, Gouvêa MEV, Siervo A, Silva MLCP, et al. Tannin-based carbon xerogel as a promising co-catalyst for photodegradation processes based on solar light: a case study using the tin (IV) oxide/carbon xerogel composite. *Chem Eng Commun.* 2021;0(0):1-13. <http://dx.doi.org/10.1080/00986445.2021.1978076>
26. Makuła P, Pacia M, Macyk W. How to correctly determine the band gap energy of modified semiconductor photocatalysts based on UV-Vis Spectra. *J Phys Chem Lett.* 2018;9(23):6814-7.
27. Pirhashemi M, Habibi-Yangjeh A, Rahim Pouran S. Review on the criteria anticipated for the fabrication of highly efficient ZnO-based visible-light-driven photocatalysts. *J Ind Eng Chem.* 2018;62:1-25. <http://dx.doi.org/10.1016/j.jiec.2018.01.012>
28. Bessekhoud Y, Robert D, Weber JV. Bi 2 S 3 / TiO 2 and CdS / TiO 2 heterojunctions as an available configuration for photocatalytic degradation of organic pollutant. *J Photochem Photobiol Chem.* 2004;163:569-80.
29. Ma A, Tang Z, Shen S, Zhi L, Yang J. Controlled synthesis of  $\text{ZnxCd1-xS}$  nanorods and their composite with RGO for high-performance visible-light photocatalysis. *RSC Advances.* 2015;5(35):27829-36.
30. Moraes NP, Torezin FA, Dantas GVJ, de Sousa JGM, Valim RB, Rocha RS, et al.  $\text{TiO}_2/\text{Nb}_2\text{O}_5/\text{carbon}$  xerogel ternary photocatalyst for efficient degradation of 4-chlorophenol under solar light irradiation. *Ceram Int.* 2020;46(10):14505-15. <http://dx.doi.org/10.1016/j.ceramint.2020.02.249>
31. Xu J, Liu Y, Li X, Chen M. Construction of Z-scheme  $\text{Bi}_3\text{TaO}_7/\text{Zn}_{0.5}\text{Cd}_{0.5}\text{S}$  composites with high efficiency for levofloxacin degradation under visible light irradiation. *Dalton Trans [serial on the Internet].* 2021 [cited 2022 Jan 21];50(41):14920-31. Available from: <https://pubs.rsc.org/en/content/articlehtml/2021/dt/d1dt02539b>
32. Nasir JA, Rehman ZU, Shah SNA, Khan A, Butler IS, Catlow CRA. Recent developments and perspectives in CdS-based photocatalysts for water splitting. *J Mater Chem A Mater Energy Sustain.* 2020;8(40):20752-80.
33. Nosaka Y, Nosaka AY. Generation and detection of reactive oxygen species in photocatalysis. *Chem Rev.* 2017;117(17):11302-36.
34. Elghniji K, Hentati O, Mlaik N, Mahfoudh A, Ksibi M. Photocatalytic degradation of 4-chlorophenol under P-modified  $\text{TiO}_2/\text{UV}$  system: kinetics, intermediates, phytotoxicity and acute toxicity. *J Environ Sci.* 2012;24(3):479-87. [http://dx.doi.org/10.1016/S1001-0742\(10\)60659-6](http://dx.doi.org/10.1016/S1001-0742(10)60659-6)
35. Pieper DH, Pollmann K, Nikodem P, Gonzalez B, Wray V. Monitoring key reactions in degradation of chloroaromatics by in situ <sup>1</sup>H nuclear magnetic resonance: solution structures of metabolites formed from cis-dienelactone. *J Bacteriol.* 2002;184(5):1466-70.